 Open access • Journal Article • DOI:10.1061/(ASCE)EM.1943-7889.0001043

## Basic Mechanical Properties of Wet Granular Materials: A DEM Study

— [Source link](#) 

[Vinh-Du Than](#), [Saeed Khamseh](#), [Anh Minh Tang](#), [Jean-Michel Pereira](#) ...+2 more authors

**Published on:** 01 Jan 2017 - [Journal of Engineering Mechanics-asce](#) (American Society of Civil Engineers)

**Topics:** [Shear stress](#), [Shear rate](#), [Granular material](#), [Capillary bridges](#) and [Capillary action](#)

Related papers:

- [Flow of wet granular materials: A numerical study.](#)
- [A Theoretical Study of the Liquid Bridge Forces between Two Rigid Spherical Bodies](#)
- [Shear strength properties of wet granular materials.](#)
- [Stress transmission in wet granular materials.](#)
- [Capillary Bridges between Two Spherical Bodies](#)

Share this paper:    

View more about this paper here: <https://typeset.io/papers/basic-mechanical-properties-of-wet-granular-materials-a-dem-sha2uuiicvo>



**HAL**  
open science

# Basic Mechanical Properties of Wet Granular Materials: A DEM Study

Vinh Du Than, Saeed Khamseh, Anh Minh Tang, Jean-Michel Pereira,  
François Chevoir, Jean-Noël Roux

► **To cite this version:**

Vinh Du Than, Saeed Khamseh, Anh Minh Tang, Jean-Michel Pereira, François Chevoir, et al.. Basic Mechanical Properties of Wet Granular Materials: A DEM Study. *Journal of Engineering Mechanics - ASCE*, American Society of Civil Engineers, 2017, 143 (1), 10.1061/(ASCE)EM.1943-7889.0001043 . hal-01515873

**HAL Id: hal-01515873**

**<https://hal-enpc.archives-ouvertes.fr/hal-01515873>**

Submitted on 3 May 2017

**HAL** is a multi-disciplinary open access archive for the deposit and dissemination of scientific research documents, whether they are published or not. The documents may come from teaching and research institutions in France or abroad, or from public or private research centers.

L'archive ouverte pluridisciplinaire **HAL**, est destinée au dépôt et à la diffusion de documents scientifiques de niveau recherche, publiés ou non, émanant des établissements d'enseignement et de recherche français ou étrangers, des laboratoires publics ou privés.

# BASIC MECHANICAL PROPERTIES OF WET GRANULAR MATERIALS: A DEM STUDY

Vinh Du Than<sup>1</sup>, Saeed Khamseh<sup>1</sup>,

Anh Minh Tang<sup>1</sup>, Jean-Michel Pereira<sup>1</sup>, François Chevoir<sup>1</sup>, Jean-Noël Roux<sup>1</sup>

## ABSTRACT

We use discrete, grain-level numerical simulations of a model granular assembly, made of spherical balls, to investigate the influence of a small amount of an interstitial wetting liquid, forming capillary bridges between adjacent particles, on two basic aspects of granular material rheology: (i) the plastic response in isotropic compression, and (ii) the critical state under monotonic shear strain, and its generalization to steady, inertial flow. Tensile strength  $F_0 = \pi\Gamma a$ , in contacts between beads of diameter  $a$  joined by a small meniscus of a liquid with surface tension  $\Gamma$ , introduces a new force scale and a new dimensionless control parameter,  $P^* = a^2P/F_0$ , for grains of diameter  $a$  under confining stress  $P$ . Under low  $P^*$ , as cohesion dominates, capillary cohesion may stabilize very loose structures. Upon increasing pressure  $P$  in isotropic compression, such structures gradually collapse. The resulting irreversible compaction is well described by the classical linear relation between  $\log P^*$  and void ratio in some range, until a dense structure forms which retains its stability without cohesion as confinement dominates for large  $P^*$ . In steady shear flow, with uniform velocity gradient  $\dot{\gamma} = \frac{\partial v_1}{\partial x_2}$  under normal stress  $P = \sigma_{22}$ , the apparent internal friction coefficient, which we define as  $\mu^* = \frac{\sigma_{12}}{\sigma_{22}}$ , depends on  $P^*$  and inertial number (reduced shear rate)  $I = \dot{\gamma} \sqrt{\frac{m}{aP}}$ , and so does solid fraction  $\Phi$ . The material exhibits, as  $P^*$  decreases, a strongly enhanced resistance to shear (larger  $\mu^*$ ). In the quasistatic limit, for  $I \rightarrow 0$ , it is roughly predicted by a simple effective pressure assumption, by which the capillary forces are deemed equivalent to

---

<sup>1</sup>Université Paris Est, Laboratoire Navier, 2 Allée Kepler, Cité Descartes, 77420 Champs-sur-Marne, France

23 an isotropic pressure increase applied to the dry material, as long as  $P^* \geq 1$ , while the yield  
24 criterion approximately assumes the Mohr-Coulomb form. At lower  $P^*$ , such models tend to  
25 break down as liquid bonding, causing connected clusters to survive over significant strain  
26 intervals, strongly influences the microstructure. Systematic shear banding is observed at  
27 very small  $P^*$ .

28 **Keywords:** granular materials, cohesion, capillary forces, effective pressure, Mohr-Coulomb,  
29 DEM

## 30 INTRODUCTION

31 Over the last decades our understanding of the microstructural and micromechanical  
32 origins of macroscopic granular material rheology have greatly benefitted from the devel-  
33 opment of numerical simulation methods of the so-called discrete element type (DEM), in  
34 which the motions and interactions of individual grains are modeled (Radjaï and Dubois  
35 2011). In particular, two basic concepts, which had previously been identified and exploited  
36 in process, chemical and geomechanical engineering, were revisited, and supported by mi-  
37 cromechanical interpretations. One is the *random close packing (RCP) state* (Cumberland  
38 and Crawford 1987), the configuration of a granular assembly maximizing density under the  
39 constraint of mutual non-interpenetrability of the grains, without any specific ordering. The  
40 RCP state is a stable equilibrium state of an isotropically compressed assembly of rigid,  
41 frictionless grains (Agnolin and Roux 2007a; Donev et al. 2005; O’Hern et al. 2003), and  
42 its characteristics, most notably its solid fraction, are remarkably reproducible, irrespective  
43 of the dynamical assembling method. Furthermore, because frictionless particle assemblies  
44 appear to be devoid of dilatancy – which has been explicitly checked for disks and spherical  
45 beads (Peyneau and Roux 2008a), and for polygonal shapes in 2D (Azéma et al. 2015) – the  
46 same solid fraction (about 0.64 for identical beads) is obtained on preparing, without any  
47 friction mobilization, packings under different, possibly anisotropic, conditions (Silbert et al.  
48 2002; Peyneau and Roux 2008b). In the presence of friction, many different states can be ob-  
49 served, varying in density and coordination number (Agnolin and Roux 2007a; Magnanimo

50 et al. 2008), even if stresses and microstructure are isotropic. The second traditional notion  
51 which has been revisited by DEM, with due attention to its microscopic foundations, is that  
52 of the *critical state*, in the sense of soil mechanics (Wood 1990; Mitchell and Soga 2005): the  
53 steady state of plastic flow attained, irrespective of the initial state, after large enough strain  
54 in monotonically, quasistatically sheared material. The critical state has been shown (Radjaï  
55 et al. 2004; Rothenburg and Kruyt 2004; Radjaï et al. 2012; Kruyt and Rothenburg 2014)  
56 to be an attractor state for all variables characterizing internal structure, micromorphology  
57 and forces, such as coordination numbers, fabric tensors or friction mobilization, as well  
58 as for stresses and solid fraction. Upon increasing the shear rate, the material behavior is  
59 affected by inertial effects, and the internal state of the homogeneously sheared material  
60 depends, under controlled normal stress  $P$ , on inertial number  $I$  (as defined in the abstract),  
61 the quasi-static critical state corresponding to the limit of  $I \rightarrow 0$ . This generalization of the  
62 critical state to  $I$ -dependent steady homogeneous shear flows has led to the formulation of  
63 efficient constitutive laws for dense granular flows (Forterre and Pouliquen 2008; Andreotti  
64 et al. 2013), in terms of the  $I$  dependence of internal friction coefficient  $\mu^*$  and solid frac-  
65 tion  $\Phi$ . The RCP state (or another well-controlled homogeneous isotropic packing state)  
66 on the one hand, and the critical state, on the other hand, correspond to the initial and  
67 the final states in many relevant mechanical tests – typically one starts from some isotropic  
68 packing, of which the RCP is an important limiting case, and one imposes a loading path  
69 leading to the critical state (Thornton 2000; Radjaï et al. 2004). Their interest also stems  
70 from their lack of dependence on many features and parameters governing contact behavior,  
71 especially dynamical ones, but also elastic contact stiffnesses, in the frequent case of negli-  
72 gible contact deflections (Roux and Chevoir 2011). On introducing new models for grains,  
73 with such features as rolling resistance or angularity (Azéma et al. 2013; Saint-Cyr et al.  
74 2012; Estrada et al. 2011), it is natural to first investigate microstructural and mechanical  
75 properties of RCP and critical states. Cohesive forces in contacts significantly affect both  
76 isotropic packings (Gilabert et al. 2007) and steady shear flows (Rognon et al. 2006).

77 The present paper states some essential results obtained by DEM simulations, for both  
78 isotropically compressed static assemblies, and  $I$ -dependent steady uniform shear flows, with  
79 special emphasis on the critical state in the limit of  $I \rightarrow 0$ , in the case of a model of wet  
80 spherical grains. Compared to similar numerical studies in the literature (Richefeu et al.  
81 2006; Scholtès et al. 2009b) the ones presented here investigate looser structures, which  
82 could not be observed with dry grains – as evidenced in experiments with sands (Bruchon  
83 et al. 2013a; Bruchon et al. 2013b). While both situations should be more extensively  
84 studied, in more detailed publications (Khamseh et al. 2015; Than et al. 2015), in which  
85 thorougher investigations of microscopic aspects will be presented, some salient features of  
86 isotropic compression and steady shear flows are described, stressing the differences with  
87 dry, cohesionless materials.

88 The paper is organized in the following way. Once the model material and the inter-  
89 actions are suitably described in the forthcoming section (“*Model material and simulation*  
90 *ingredients*”), the two main parts of the paper separately address these two important as-  
91 pects of wet granular material rheology: “*Isotropic assembly and compression*”, and then  
92 “*Dense shear flow and critical states*”. The final *Conclusion* section sums up the results and  
93 puts them in perspective.

## 94 **MODEL MATERIAL AND SIMULATION INGREDIENTS**

### 95 **Stress and Strain Control**

96 Our model material is an assembly of  $N$  equal-sized spherical beads of diameter  $a$ . The  
97 simulation cell is a rectangular cuboid, with edges, of lengths  $(L_\alpha)_{1 \leq \alpha < 3}$ , parallel to coordi-  
98 nate axes, periodic in all three directions. We control all three diagonal stress components in  
99 isotropic compression, and wait for equilibrium conditions, as in Agnolin and Roux (2007a),  
100 to be satisfied within a preset tolerance. In shear tests a granular flow is imposed in direction  
101 1, with a gradient in direction  $x_2$ , defining shear rate  $\dot{\gamma} = \frac{\partial v_1}{\partial x_2}$ . In that case, the periodic-  
102 ity in direction 2 is implemented through the Lees-Edwards procedure (Allen and Tildesley

103 1987), length  $L_2$  is allowed to vary in response to the enforced condition of constant normal  
 104 stress  $\sigma_{22}$ , while lengths  $L_1$  and  $L_3$  are kept fixed – as in Peyneau and Roux (2008a).

### 105 **Force Model: Elasticity and Friction**

106 The spherical beads are assumed to be made of a material with Young modulus  $E$   
 107 and Poisson ratio  $\nu$ . Coulomb friction applies in the contacts, with friction coefficient  $\mu$ .  
 108 Elastic-frictional contact forces are modeled with a simplified Hertz-Mindlin-Deresiewicz  
 109 force law (Agnolin and Roux 2007a). The normal Hertz force  $F_N$  depends on contact deflec-  
 110 tion  $h$  as

$$111 F_N = \frac{\tilde{E}\sqrt{a}}{3}h^{3/2}, \quad (1)$$

112 in which we introduced notation  $\tilde{E} = E/(1 - \nu^2)$ . The adopted simplified form of tangential  
 113 elasticity (Agnolin and Roux 2007a) involves a constant ratio  $(2 - 2\nu)/(2 - \nu)$  of tangential  
 114 ( $K_T$ ) to normal ( $K_N$ ) stiffnesses in contacts. Both depend on  $F_N$ , as, from (1),  $K_N = \frac{dF_N}{dh} \propto$   
 115  $F^{1/3}$ . With such laws one should avoid spurious creation of elastic energy, and therefore  $K_T$   
 116 is suitably rescaled in cases of decreasing normal force (Elata and Berryman 1996). Details  
 117 on the elastic model, on the enforcement of the Coulomb condition,

$$118 \|\mathbf{F}_T\| \leq \mu F_N, \quad (2)$$

119 and on the objective implementation of the force law, with due account of all possible motions  
 120 of a pair of contacting grains, are given by Agnolin and Roux (2007a). Our simulations are  
 121 carried out with the elastic properties of glass beads ( $\tilde{E} = 77$  GPa) and the intergranular  
 122 friction coefficient,  $\mu$ , is kept equal to 0.3 in the present study.

123 Estimating the typical contact deflection under confining stress  $P$  leads to the definition  
 124 of a dimensionless stiffness parameter  $\kappa$  (Radjaï and Dubois 2011), such that  $h/a \propto \kappa^{-1}$ .  
 125 For a Hertzian contact, one may use (Agnolin and Roux 2007a)

$$126 \kappa = \left(\frac{\tilde{E}}{P}\right)^{2/3}. \quad (3)$$

127 In our shear test simulations we keep  $\kappa = 8400$ , corresponding to glass beads under pressure  
 128 100 kPa. It is deemed large enough to approach the limit of rigid grains with good accuracy.

129 Viscous damping terms oppose normal relative motion of contacting grains, and are  
 130 chosen to correspond to a restitution coefficient close to zero in normal collisions. Such terms  
 131 were shown (da Cruz et al. 2005; Peyneau and Roux 2008a) to have negligible influence in  
 132 the slow compression steps and shear flows of the present study.

### 133 **Force Model : Capillary Attraction**

134 An interstitial wetting liquid, introduced in small amounts, preferentially localizes at  
 135 contacts or between close neighboring grains, forming liquid bridges transmitting capillary  
 136 forces. Such a liquid bridge, or meniscus, is sketched in Fig. 1. We consider a perfectly wet-  
 137 ting liquid, with contact angle  $\theta$  equal to zero. In accordance with some observations (Her-  
 138 minghaus 2005), we assume that the menisci only form as particles come into contact. If  
 139 contacting grains move apart from one another, and are separated by distance  $h$ , the liquid  
 140 bridge remains stable, transmitting an  $h$ -dependent force, until the gap,  $h$ , reaches a certain  
 141 rupture distance  $D_0$ , as observed in (Kohonen et al. 2004).  $D_0$  relates to meniscus volume  
 142  $V$  as  $D_0 \simeq V^{1/3}$  (Lian et al. 1993; Willett et al. 2000; Pitois et al. 2000).

143 The attractive force between particles separated by distance  $h \leq D_0$  is modeled within  
 144 the Maugis approximation (Maugis 1987), appropriate for small enough meniscus volume.  
 145 The maximum attractive force (tensile strength) is reached for contacting particles, and  
 146 equal, according to this model, to  $F_0 = \pi a \Gamma$  ( $\Gamma$  is the liquid surface tension) independent of  
 147 the meniscus volume. The capillary force varies with gap  $h$  between particle surfaces as

$$148 \quad F^{\text{Cap}} = \begin{cases} -F_0 & h \leq 0 \\ -F_0 \left[ 1 - \frac{1}{\sqrt{1 + \frac{2V}{\pi a h^2}}} \right] & 0 < h \leq D_0 \\ 0 & h > D_0 \end{cases} \quad (4)$$

149 (One should note that  $h < 0$  corresponds to an elastic deflection of the particles in contact,



150 and keep in mind that a nonvanishing distant force,  $F^{\text{Cap}}(h)$  with  $h > 0$ , is only possible  
151 if the grains have been in contact and did not move apart farther than distance  $D_0$  ever  
152 since). This formula is a simpler, analytical form of the toroidal approximation with the  
153 “gorge method” (Lian et al. 1993) for the capillary force in a meniscus. Alternative forms  
154 of the attractive force law (Willett et al. 2000; Soulié et al. 2006; Radjaï and Richefeu 2009)  
155 might actually be more accurate. We found (Khamseh et al. 2015) that the macroscopic  
156 results were not affected upon changing the force law, were very moderately influenced  
157 by saturation within the pendular range, but did significantly change upon suppressing the  
158 capillary hysteresis (i.e., assuming menisci to form as soon as a pair of grains approach within  
159 rupture distance  $D_0$ ). It is important to recall that the Coulomb inequality, as written in (2),  
160 applies to the elastic component of the normal force only, to which the negative (attractive)  
161 capillary term should be added. Thus, in an isolated grain pair bonded by a meniscus,  
162 at equilibrium the repulsive elastic force is equal to  $F_0$ , and the contact may transmit a  
163 tangential force at most as large as  $\mu F_0$ .

164 The morphology of partially saturated granular materials depends on the liquid con-  
165 tent (Mitarai and Nori 2006; Kudrolli 2008). The present study, like a number of previous  
166 ones (Richefeu et al. 2006; Radjaï and Richefeu 2009; Scholtès et al. 2009a), is restricted to  
167 the *pendular state* of low saturations, in which the wetting liquid is confined in bonds or  
168 menisci joining contacting grains. Liquid saturation  $S$  is defined as the ratio of liquid volume  
169  $\Omega_l$  to interstitial volume  $\Omega_v$ , the total system volume being denoted as  $\Omega$ . Writing  $\Omega_g$  for the  
170 volume of all  $N$  solid grains in the system (such that  $\Omega = \Omega_g + \Omega_v$ ,  $S$  is related to meniscus  
171 volume  $V$ , solid fraction  $\Phi = \Omega_g/\Omega = 1 - \Omega_v/\Omega = \frac{N\pi a^3}{6\Omega}$  and wet coordination number  $z$  (the  
172 average number of liquid bonds on one grain). As the liquid volume is  $\Omega_l = \frac{zNV}{2}$ , one has

$$173 \quad S = \frac{\Omega_l}{\Omega_v} = \frac{zNV}{2(1 - \Phi)\Omega} = \frac{3z}{\pi} \frac{\Phi}{1 - \Phi} \frac{V}{a^3}. \quad (5)$$

174 In our study, we fix the value of meniscus volume  $V$ , equal to  $10^{-3}a^3$  in all results presented

175 in this paper. Such a choice does not conserve the total liquid volume (proportional to the  
 176 varying coordination number  $z$  of liquid bonds) – but this is, as we could check (Khamseh  
 177 et al. 2015), quite an innocuous drawback.

178 The pendular state to which our model applies is relevant in some low (but not too  
 179 small) saturation range. The upper saturation limit for the pendular state corresponds to the  
 180 merging of the menisci pertaining to the same grain, which, considering a triangle of spherical  
 181 grains in mutual contact, happens as soon as the filling angle  $\varphi$  (see Fig. 1) reaches  $\pi/6$ . The  
 182 analytical formula for  $V$  (Lian et al. 1993), within the toroidal approximation, as a function  
 183 of  $\varphi$  (setting  $h = 0$ , and  $\theta = 0$ ), then yields  $\frac{V}{a^3} \simeq 8.10^{-3}$ . Eq. (5) then predicts a maximum  
 184 saturation between 0.05 and 0.1, similar to experimental observations (Herminghaus 2005;  
 185 Mitarai and Nori 2006). On the other hand, the minimum saturation  $S_{\min}$  for bridges to  
 186 form and join neighbouring grains might be roughly estimated upon introducing a roughness  
 187 scale  $\delta$ , assuming a liquid layer of thickness  $\delta$  coats the surface of the grains, as

$$188 \quad S_{\min} = \frac{6\Phi\delta}{(1-\Phi)a}. \quad (6)$$

189 For  $\Phi = 0.5$  and  $\delta \sim 10^{-4}a$ ,  $S_{\min}$  is of the order of  $10^{-3}$ , as observed in experiments (Her-  
 190 minghaus 2005). Using (5), and typical values of  $z$  and  $\Phi$ , this sets a lower bound to meniscus  
 191 volume, of order  $10^{-4}a^3$ .

192 Capillary attraction introduces force scale  $F_0$  in the model, whence the definition of a  
 193 reduced pressure, comparing applied stress  $P$  (isotropic pressure in compression, or controlled  
 194 normal stress  $\sigma_{22} = P$  for shear flows) to contact tensile strength  $F_0$ , as

$$195 \quad P^* = \frac{a^2 P}{F_0} = \frac{aP}{\pi\Gamma}. \quad (7)$$

196 As observed with different cohesive granular models, mostly in two dimensions (2D) (Gilabert  
 197 et al. 2007), we expect strong effects of cohesive forces, possibly very loose equilibrium  
 198 microstructures for  $P^* \ll 1$ , while the properties of cohesionless systems are retrieved in the

199 limit of large  $P^*$ . Our simulations are carried out with spheres of diameter  $a = 0.115$  mm,  
200 perfectly wet by water, with surface tension  $\Gamma = 7.3 \times 10^{-2}$  J.m<sup>-2</sup>. For such parameter  
201 values, one has  $P^* = 1$  for a pressure  $P$  equal to 2 kPa. While this is admittedly a rather  
202 low pressure for most geotechnical applications, it might be relevant in other fields (e.g.,  
203 in some chemical engineering process), and the results are also, beyond wet grain models,  
204 more generally indicative of the influence of attractive forces of small range in granular  
205 assemblies. Another important issue is the possible influence of the initial microstructure  
206 assembled under low  $P^*$  on the material properties under larger confining stresses. In the  
207 following most results are expressed in terms of dimensionless control parameters.

## 208 **ISOTROPIC ASSEMBLY AND COMPRESSION**

209 We studied the important irreversible configuration changes entailed by a pressure cycle  
210 starting with a low value of  $P^*$ , of order  $10^{-2}$  or  $10^{-3}$ , with an initial state that cannot  
211 be observed without cohesive forces. Maximum pressures are such that  $P^* \gg 1$ . Our  
212 parameter choice is such that  $\kappa = 114000$  for  $P^* = 1$  and  $\kappa = 5300$  for  $P^* = 100$ , which is  
213 still high enough a value for contact deflections to be irrelevant (Roux and Chevoir 2011).  
214 Consequently, our results, if expressed as dimensionless quantities functions of  $P^*$  ( $\kappa$  being  
215 large enough to be irrelevant), may apply to systems of wet spherical grains with arbitrary  
216 diameter, liquid surface tension and wetting angle.

### 217 **Loose initial states**

218 Previous 2D simulations of cohesive systems by Gilabert et al. (2007) made it clear  
219 that cohesive forces play an important part in the assembling stage. It is thus necessary to  
220 assemble wet grains, rather than introduce liquid bridges into previously assembled dry grain  
221 configurations. As in the 2D studies, we found it possible to assemble low density initial  
222 configurations by the following procedure. First, disordered assemblies of grains (comprising  
223 4000 particles) with solid fraction  $\Phi_0$  are prepared, using either random insertion or crystal  
224 melting with event-driven, energy-preserving dynamics (Agnolin and Roux 2007a). Then,  
225 particles are attributed random velocities, drawn according to a Gaussian distribution with

226 zero mean and variance  $V_0^2$ , and left to interact with the force laws introduced in the previous  
 227 section, within a periodic simulation cell of fixed size and shape. Capillary attraction induces  
 228 the formation of clusters of grains joined by liquid bridges, and this step of the calculation is  
 229 stopped when all particles belong to one single such cluster, and the configuration is regarded  
 230 as sufficiently equilibrated. (Tolerances on equilibrium requirements are expressed in terms  
 231 of typical contact force  $F_1$  as,  $10^{-4}F_1$  for force balance, or  $10^{-4}aF_1$  for torque balance – with  
 232  $F_1 = F_0$  in the assembling stage). The structure of such initial configurations depends on  
 233 imposed solid fraction  $\Phi_0$ , which we chose equal to 0.3 in the main simulation series. It  
 234 also depends on velocity  $V_0$ . The latter should be compared to the characteristic velocity  
 235  $V^* = \sqrt{\frac{D_0 F_0}{m}}$ , which is proportional to the relative velocity that is necessary to separate  
 236 a pair of grains, overcoming the potential energy of capillary force (4). Here, choosing  
 237  $V_0/V^* = 0.2$ , we could observe that the results corresponded to a low initial agitation limit.  
 238 An important variable characterizing equilibrium configurations, the contact coordination  
 239 number,  $z_c$ , is then barely larger than 4 – the isostatic (barely rigid) value (Agnolin and  
 240 Roux 2007a). The coordination number of distant interactions, i.e., the average number of  
 241 non-contacting neighbors connected to one grain through a capillary meniscus, which we  
 242 denote as  $z_d$ , is equal to zero. This latter observation is explained by the capillary hysteresis:  
 243 liquid bonds without contact only exist in pairs that have been in contact in the past. Thus,  
 244 for low enough initial agitation velocity  $V_0$ , contacts, once formed in the assembling stage,  
 245 do not break in the constant density aggregation stage.

## 246 **Compression curves**

### 247 *Loading procedure and measurements*

248 To study the compression of initially loose configurations, stabilized at  $\Phi_0 = 0.3$  thanks to  
 249 adhesive forces, a loading program is applied in which the isotropic pressure,  $P$ , is stepwise  
 250 incremented, from a low value (corresponding to  $P^* = 10^{-3}$ ) up to  $P^* = 10000$ . Steps  
 251 are uniform on a logarithmic scale (i.e., pressure is multiplied by  $10^{1/4}$  at each step). For  
 252 each new value of applied pressure  $P$ , one waits for equilibrium to be approached with good

253 accuracy, and records the new configuration. To appreciate the irreversibility of the observed  
254 evolution, the loading program is a compression cycle with a decompression branch, on which  
255 the previously applied pressure levels are retraced back, down to the initial small value. This  
256 paper being only a brief account of salient behaviours in compression and in quasistatic shear  
257 flow, we do not present here a complete study of all properties and internal states of  $P^*$ -  
258 dependent isotropic configurations. We mainly focus on solid fraction  $\Phi$ , or, according to  
259 the soil mechanics presentation, on void ratio  $e = -1 + 1/\Phi$ , and on contact ( $z_c$ ) and distant  
260 ( $z_d$ ) coordination numbers. A more complete parametric study (dependence on velocity  
261  $V_0$ , meniscus volume, or various aspects of interaction laws such as capillary hysteresis and  
262 possible rolling friction) is also postponed to a forthcoming, more detailed publication (Than  
263 et al. 2015).

#### 264 *Irreversible compression*

265 Fig. 2(a) shows the evolution of the void ratio in the isotropic compression of a system  
266 of 4000 beads, with the characteristics as described in the previous sections. The loading  
267 curve is composed of three parts: first (regime I), in range  $P^* \leq 0.01$ , the initial structure  
268 supports the pressure increase, and void ratio  $e$  hardly departs from its initial value (equal to  
269 2.33). Then, in a second stage (regime II), extending up to  $P^* \simeq 10$ , the system undergoes  
270 a fast compression, which becomes considerably slower at high pressures (regime III). On  
271 reducing  $P^*$ , only the density change occurring within regime III is reversed. As apparent  
272 on the second graph, Fig. 2(b), in which the reference wet system is compared to a dry  
273 (cohesionless) assembly of identical grains, regime III is parallel to the compression curve  
274 of dry grains, in which the small compression is due to contact elasticity, and, as shown by  
275 Agnolin and Roux (2007b), nearly reversible (in terms of density at least). Thus regime III  
276 marks the end of the plastic collapse of the loose structure stabilized by capillary forces.

277 The plastic compression behavior of the wet material is closely similar to the 2D results  
278 of Gilabert et al. (2008), and the void ratio curve in regime II might be represented with  
279 a linear variation with  $\log P^*$ , assuming  $e_{\text{ref}}$  is the void ratio for some reference reduced

280 pressure,  $P_{\text{ref}}^*$ :

$$281 \quad e - e_{\text{ref}} = -\lambda \log \frac{P^*}{P_{\text{ref}}^*}. \quad (8)$$

282 Coefficient  $\lambda \simeq 0.36$  successfully describes the curve in interval  $0.04 \leq P^* \leq 2$ . Eq. 8 is clas-  
283 sically used in soil mechanics for cohesive systems (Mitchell and Soga 2005). Upon unloading  
284 and reloading at various pressure levels along the compression curve, it is observed (as shown  
285 in Fig. 3) that a plastic response (irreversible structural rearrangement with density change)  
286 under isotropic pressure will be observed only if the maximum pressure the system has been  
287 subjected to in the past (the “overconsolidation pressure” of soil mechanics) is exceeded.  
288 This maximum pressure value appears to fully characterize the history dependence of the  
289 system in isotropic compression.

### 290 *Coordination numbers*

291 In the compression cycle, the coordination numbers of contact ( $z_c$ ) and distant ( $z_d$ ) inter-  
292 actions are shown in Fig. 4. Compared to density changes, those of the contact coordination  
293 number are remarkably small, as it increases from nearly 4 to about 4.8 after the full pres-  
294 sure cycle. As to the coordination number of menisci between distant grains, it starts at  
295 zero, due to the absence of contact opening in the assembling stage with small agitation  
296 velocity. Its increase to 2 in the course of irreversible compression signals the failure of the  
297 contact structure: the network gets rearranged as old contacts break, and are replaced by  
298 menisci connecting receding grain pairs, and new contacts form. The small change in  $z_c$  is  
299 the net effect of contact creations and destructions. The final increase of  $z_c$ , accompanied by  
300 a decrease of  $z_d$ , in regime III (high pressures) is caused by the elastic compression, closing  
301 the gaps between non-contacting pairs, as in dry systems (Agnolin and Roux 2007b). We  
302 could check that the coordination numbers remain very nearly constant along the reversible  
303 paths of Fig. 3, which corresponds to unperturbed contact and meniscus networks.

304 Because of the capillary hysteresis of meniscus formation and breakage, only a proportion  
305 of neighbour pairs within rupture distance  $D_0$  (defined in the presentation of the force model,

306 in connection with Eq. 4), are connected by a liquid bridge. This proportion is initially zero,  
307 it increases with  $P^*$ , peaking at 70% in regime II, decreasing to about 55% in the denser  
308 systems (similar to the value  $\sim 50\%$  reported in the experiments by Kohonen et al. (2004)).

### 309 *Effect of drying or of saturating*

310 In practice, one may act on a wet system by changing its saturation. The most drastic  
311 change should be obtained on entirely suppressing the capillary cohesion, either by drying,  
312 or by completely saturating the intergranular voids by the liquid. In numerical simulations,  
313 one may simply remove all capillary forces, leaving only the interactions present in a dry  
314 system. It is interesting to observe the effects of such an ideal transformation, carried out  
315 at various points along the irreversible compression curve. Fig. 5 shows the resulting void  
316 ratio evolution, if the system is deprived of capillary forces immediately before unloading at  
317 different pressure levels. This ideal drying or saturation step produces a sudden collapse (a  
318 brutal compression step), unless all irreversible compression has already taken place (as for  
319 points F and G on Fig. 5). (More gradual collapse due to progressive imbibition is reported  
320 in some experiments (Bruchon et al. 2013b)). In such a case, one may remove all capillary  
321 forces, as their mechanical role, at high  $P^*$ , is negligible. Remarkably, the final state after  
322 decompression keeps the same density, whether or not the system has been deprived of  
323 capillary cohesion.

## 324 **DENSE SHEAR FLOW AND CRITICAL STATE**

### 325 **Model Parameters**

326 The results reported here pertain to the same reference systems studied in isotropic  
327 compression, with  $N = 4000$ , friction coefficient  $\mu = 0.3$  in the contacts, meniscus volume  
328  $V = 10^{-3}a^3$ . While stiffness number  $\kappa$  is fixed, reduced pressure takes values  $P^* = \infty$  (i.e.,  
329 the dry case), 10, 5, 2, 1, 0.436 and 0.1. The investigated range of  $I$  values (varying from  
330  $10^{-4}$  to 0.562 by factors of  $\sqrt{10}$ ) enables an accurate determination of the quasistatic limit,  
331 as well as an assessment of inertial effects.

332 We focus on situations in which a uniform steady state might be identified under constant  
 333 macroscopic shear rate  $\dot{\gamma}$ , after a transient stage (of a few unit strains at most). This turns out  
 334 to exclude small values of  $P^*$ : we could record homogeneous state parameters for  $P^* = 0.436$ ,  
 335 but only partial information was gathered on the material state under  $P^* = 0.1$ , since such  
 336 systems flow inhomogeneously, localizing the velocity gradient within a narrow shear band  
 337 (save for a restricted range of  $I$  values of order 0.01).

### 338 Constitutive laws

339 Restricting their measurement to the higher values of  $P^*$ , we measure the (apparent)  
 340 macroscopic friction coefficient  $\mu^* = \frac{\sigma_{12}}{\sigma_{22}}$ , and solid fraction  $\Phi$ , in steady homogeneous shear  
 341 flows, with the results shown in Fig. 6. As in some published results (Rognon et al. 2006;  
 342 Rognon et al. 2008), obtained in 2D with a model of cohesive disks, lower  $P^*$  values increase  
 343  $\mu^*$  and decrease the density of the sheared material. One may note, though, that the effect  
 344 on  $\mu^*$  is considerably larger in the 3D assembly of wet particles: even for  $P^* = 1$ , when the  
 345 attractive forces and the confining ones are of similar magnitude, the quasistatic internal  
 346 friction coefficient, compared to its dry value ( $P^* = \infty$ ),  $\mu_0^\infty = 0.335$ , nearly doubles, at  
 347 about 0.61. It reaches  $0.867 \pm 0.003$  at  $P^* = 0.436$ . In addition to the values shown in the  
 348 figure, limited data are available for  $P^* = 0.1$ , in a range of  $I$  (of order 0.01) for which shear  
 349 banding does not occur. Such  $I$  values are close enough, judging from the  $I$  dependence of  
 350  $\mu^*$  at different  $P^*$  levels, to the quasistatic limit of  $I \rightarrow 0$ . We could then measure  $\mu^* \simeq 1.62$   
 351 and  $\Phi \simeq 0.435$ .

352 As suggested by Rognon et al. (2006), for each  $P^*$ , a power law fit can describe the  $I$   
 353 dependence of  $\mu^*$  and  $\Phi$ , as in a number of studies of dry granular flows (Hatano 2007;  
 354 Peyneau and Roux 2008a):

$$355 \mu^* = \mu_0^* + CI^\alpha \quad (9)$$

356 The data are compatible with a  $P^*$ -independent value of exponent  $\alpha$ ,  $\alpha \simeq 0.8$ , while coeffi-  
 357 cient  $C$  decreases for smaller  $P^*$ . In comparison with  $\mu^*$ , the solid fraction changes relatively



358 little as a function of both  $P^*$  and  $I$  in the investigated range. Both quantities tend to depart  
 359 slower from their quasistatic limit for  $I \rightarrow 0$  as cohesive effects get stronger (for smaller  $P^*$ ).

360 Void ratios  $e_0 = -1 + 1/\Phi_0$  in the  $P^*$ -dependent critical states are compared to the  
 361 values  $e_{\text{iso}}(P^*)$  obtained in direct isotropic compression (normally consolidated states) in  
 362 Fig. 7. The difference  $e_{\text{iso}} - e_0$  is a decreasing function of  $P^*$ , but remains positive, and  
 363 critical states are denser than isotropically compressed ones (this also applies to dry grains,  
 364  $P^* = \infty$  – see the inserted subplot of Fig. 7). All normally consolidated isotropic states  
 365 should therefore be regarded as loose: they have to contract under shear before approaching  
 366 the critical state.

## 367 **Internal States, Microscopic Aspects**

### 368 *Coordination numbers*

369 Coordination numbers are shown in Fig. 8, as functions of  $P^*$  for different  $I$ , showing  
 370 a quasistatic limit to be closely approached at small  $I$ . A comparison to isotropic states  
 371 obtained in compression (Fig. 4) reveals, unlike for the density, quite similar values of both  
 372  $z_c$  and  $z_d$  at given  $P^*$ . The number of contacts does not change much with  $P^*$ , while the  
 373 number of distant interactions tends to increase with  $P^*$ . Faster flows (larger  $I$  values) tend  
 374 to break contacts, which results in smaller  $z_c$  values, an effect partly compensated by the  
 375 increase of  $z_d$ : menisci survive contact openings with separation distances below  $D_0$ .

### 376 *Contributions to stresses*

377 Throughout the studied parameter range, stresses in the flow are dominated by force  
 378 contributions:

$$379 \quad \sigma_{\alpha\beta} = \frac{1}{\Omega} \sum_{i < j} F_{ij}^{\alpha} r_{ij}^{\beta}, \quad (10)$$

380 the sum running over all pairs  $i, j$  of grains interacting by force  $F_{ij}$ ,  $r_{ij}$  pointing from the  
 381 center of  $i$  to the center of  $j$ . This suggests a decomposition into contributions of different  
 382 interactions. One may, e.g., isolate the contribution of distant interactions ( $\sigma_{\alpha\beta}^d$ ) and contact  
 383 interactions ( $\sigma_{\alpha\beta}^c$ ), the latter being split into the contributions of tangential forces ( $\sigma_{\alpha\beta}^T$ ) and

384 normal ones ( $\sigma_{\alpha\beta}^{\text{N,c}}$ ):

$$385 \quad \sigma_{\alpha\beta} = \sigma_{\alpha\beta}^{\text{c}} + \sigma_{\alpha\beta}^{\text{d}} = \sigma_{\alpha\beta}^{\text{N,c}} + \sigma_{\alpha\beta}^{\text{T}} + \sigma_{\alpha\beta}^{\text{d}} \quad (11)$$

386 Alternatively, one may split force  $F_{ij}$  into its tangential and normal components, and  
 387 isolate, in the latter, the capillary force from the elastic one. This results in a decomposition  
 388 of stresses into the contribution  $\sigma_{\alpha\beta}^{\text{Ne}}$  of normal elastic forces in contacts, the one of tangential  
 389 contact forces,  $\sigma_{\alpha\beta}^{\text{T}}$ , and that of capillary forces,  $\sigma_{\alpha\beta}^{\text{cap}}$ , the latter incorporating both contacts  
 390 and distant interactions through liquid bridges:

$$391 \quad \sigma_{\alpha\beta} = \sigma_{\alpha\beta}^{\text{Ne}} + \sigma_{\alpha\beta}^{\text{T}} + \sigma_{\alpha\beta}^{\text{cap}}. \quad (12)$$

392 To understand the large values of  $\sigma_{12}$  observed at small  $P^*$ , one may use Eq. 11, in which  
 393 all terms of the sum have the same sign. Distant interactions contribute at most (for small  
 394  $P^*$ ) 8% of the sum. Tangential forces account for about 18% of the total at  $P^* = 0.436$ ,  
 395 decreasing to 10% for  $P^* = 10$ . Thus the essential contribution to shear stress is that of  
 396 normal contact forces,  $\sigma_{12}^{\text{N,c}}$ .

397 For normal stresses, it is instructive to use decomposition (12). Capillary forces are  
 398 attractive, and thus contribute negatively to  $\sigma_{22} = P$ , as shown in Fig. 9. As the contribution  
 399 of tangential forces is vanishingly small, normal elastic forces have to compensate the effect  
 400 of  $\sigma_{22}^{\text{cap}}$ , whence  $\frac{\sigma_{22}^{\text{Ne}}}{\sigma_{22}} > 3$  for  $P^* = 0.436$ . Remarkably, the contribution of capillary forces to  
 401 shear stress, which is also opposite to that of normal repulsive forces, remains modest:  $\frac{\sigma_{12}^{\text{cap}}}{\sigma_{12}}$   
 402 evolves from about  $-0.12$  at  $P^* = 0.436$  to  $-0.03$  at  $P^* = 10$ .

403 Following a number of recent micromechanical studies of granular materials (Peyneau  
 404 and Roux 2008b; Azéma and Radjaï 2014), one may relate stresses  $\sigma_{\alpha\beta}^{\text{N}}$  due to normal forces  
 405 to fabric and force anisotropy parameters, an approach that we do not pursue any further  
 406 here (more indications are provided by Khamseh et al. (2015)).

407 *Age of contacts and menisci.*

408 One remarkable feature by which systems with capillary cohesion differ in shear flow from  
409 dry granular assemblies is the distribution of contact and interaction ages, expressed in terms  
410 of strain intervals. Thus Fig. 10 shows that the same pairs of grains may stay in interaction,  
411 joined by a meniscus, over several units of strain, the more often the lower  $P^*$ . Those  
412 distribution functions decay exponentially for large values, with a characteristic time growing  
413 from  $1.1\dot{\gamma}^{-1}$  for  $P^* = 10$  to  $1.7\dot{\gamma}^{-1}$  for  $P^* = 0.436$  – contrasting with the corresponding decay  
414 time for the *contact* age distribution in a dry cohesionless system ( $P^* = \infty$ ), which is about  
415  $0.12\dot{\gamma}^{-1}$  for  $I = 0.1$ . Interestingly, contact lifetimes might also exceed a few strain units  
416 but are considerably smaller, and, unlike meniscus lifetimes, decrease for increasing  $I$  in  
417 the investigated range. Whereas pairs of dry grains tend to come into contact if oriented  
418 within the compression quadrants of the shear flow, and then separate once in the extension  
419 quadrant, grains connected by liquid bonds tend to form clusters that survive tumbling  
420 motions in the average shear flow over notable strain intervals. Upon increasing  $I$ , although  
421 contacting pairs separate more easily, they tend to remain joined by menisci. Qualitatively,  
422 such a feature might explain the slow  $I$  dependence of  $\mu^*$  and  $\Phi$  in strongly cohesive systems,  
423 and should be related to the reduced fabric anisotropy at small  $P^*$ , as well as to the influence  
424 of meniscus volume or force range  $D_0$  (Khamseh et al. 2015).

### 425 **Effective Pressure Approach**

426 Although the discussion of the different contributions to shear stress  $\sigma_{12}$  does not lead to  
427 an explanation of the observed large values of  $\mu^*$ , the large tensile contribution of capillary  
428 forces to normal stress (Fig. 9) provides a clue. One may write

$$429 \quad \sigma_{22}^{\text{cap}} = -\beta\sigma_{22}, \quad (13)$$

430 with a coefficient  $\beta$  ranging, in the quasistatic limit, from about 0.15 ( $P^* = 10$ ) to 2.1  
431 ( $P^* = 0.436$ ). (If the result for  $P^* = 0.1$  and  $I \sim 0.01$  is added  $\beta$  then reaches about 7.2).

432 Incidentally, the independence of coefficient  $\beta$  on inertia parameter  $I$  for  $I \leq 0.1$  confirms  
 433 that the rheological effect of liquid bonds is not easily disrupted by collisions in the presence  
 434 of moderate inertial effects, as noticed from the distribution of their ages in the previous  
 435 section.

436 One may invoke the concept of *effective pressure* to describe the effect of capillary forces  
 437 on the shear resistance of the material: the attractive forces create larger repulsive elastic  
 438 reactions in the contact, corresponding to an effective pressure equal to  $(1 + \beta)\mathcal{P}$ . (Note  
 439 that one ignores here the small contribution of capillary forces to shear stress). One assumes  
 440 then that the shear behavior of the material is identical to that of a dry material under  
 441 such effective normal stress  $\sigma_{22}^{\text{eff}}$ . This approach leads to the following prediction for the  
 442  $P^*$ -dependent quasistatic friction coefficient  $\mu_0^*$ :

$$443 \quad \mu_0^* = (1 + \beta)\mu_0^\infty, \quad (14)$$

444 in which  $\mu_0^\infty$  denotes the quasistatic internal friction coefficient for dry grains,  $P^* = \infty$ .

445 The performance of the simple effective pressure prediction for the  $P^*$  dependence of  $\mu_0^*$   
 446 is visualized in Fig. 11. Although the global increase of  $\mu_0^*$  is captured, it is overestimated for  
 447 the smallest  $P^*$  values ( $P^* = 1$  and below). The relative error in the prediction of  $\mu_0^*$ , using  
 448 the exact, measured value of  $\beta$ , is about 5% at  $P^* = 10$ , increasing to 20% at  $P^* = 0.436$  (and  
 449 the value of  $\mu_0^*$  for  $P^* = 0.1$ , about 1.62, from the data for  $I \sim 0.01$  is largely overestimated,  
 450 at 2.7). Thus, the effective stress approach provides a rough estimate for internal friction  
 451 increase at small  $P^*$ , but becomes inaccurate in the strong cohesion regime. It cannot be  
 452 exact for various reasons: while the mechanical properties are supposed to be the same once  
 453 effective stresses are applied to the dry material, the density is different in the dry and  
 454 the wet case (with  $\Phi$  varying between 0.525 and 0.596 as  $P^*$  grows from 0.436 to infinity);  
 455 capillary forces also contribute to shear stress, the force network is bound to be different,  
 456 etc.

## Mohr-Coulomb Model for Critical States

Coefficient  $\beta$  might actually be predicted as follows. From Eq. 10, one may relate (Agnolin and Roux 2007a) the average pressure,  $\mathcal{P} = \text{tr}\underline{\underline{\sigma}}/3$ , to the average normal force  $\langle F^N \rangle$  for all interactions, and to the average,  $\langle F^N h \rangle_d$ , over pairs in distant interaction, of the product of force by distance  $h \leq D_0$ :

$$\mathcal{P} = \frac{\Phi z}{\pi a^2} \langle F^N \rangle + \frac{\Phi z_d}{\pi a^3} \langle F^N h \rangle_d \quad (15)$$

As normal stress differences are small, ratio  $\frac{\mathcal{P}}{\sigma_{22}}$  only slightly differs from 1 (about 0.95) at small  $I$ . In formula 15, the second term of the r.h.s. might be neglected, as it contributes less than 2% of the pressure. Contacts ( $z_c$ , on average, per grain) carry capillary force  $-F_0$ , while distant forces ( $z_d$  per grain) average to a fraction of  $-F_0$ . From (15) the capillary contribution to pressure  $\mathcal{P}$  is bracketed as  $-\frac{\Phi z F_0}{\pi a^2} \leq \mathcal{P}^{\text{cap}} \leq -\frac{\Phi z_c F_0}{\pi a^2}$ , in which  $z$  denotes the total coordination number,  $z = z_c + z_d$ . Dividing by  $\sigma_{22}$ , one obtains:

$$-\frac{\Phi z}{\pi P^*} \leq \frac{\mathcal{P}^{\text{cap}}}{\sigma_{22}} \leq -\frac{\Phi z_c}{\pi P^*}. \quad (16)$$

Ignoring the small difference between  $\mathcal{P}^{\text{cap}}$  and  $\sigma_{22}^{\text{cap}}$ , (16) provides an estimate of coefficient  $\beta$  defined in (13). Thus the value of  $\beta$  for reduced pressure  $P^* = 0.436$  is predicted between 1.9 and 2.3 (and for  $P^* = 0.1$ , it should reach about 8). Relation 16 also suggests that  $\beta$  is roughly proportional to  $1/P^*$ :

$$\beta \simeq b/P^*, \quad \text{with} \quad \frac{z_c \Phi}{\pi} \leq b \leq \frac{z \Phi}{\pi}. \quad (17)$$

Given the moderate variations of coordination numbers and density with  $P^*$  in the investigated range, one might choose a constant coefficient  $b$  in (17). Eq. 14, on multiplying by  $\sigma_{22}$ , then takes the form of a Mohr-Coulomb relation:

$$\sigma_{12} = c + \mu_1^* \sigma_{22}. \quad (18)$$

479 This relation, a classical criterion for plastic failure (Wood 1990; Biarez and Hicher 1993;  
 480 Richefeu et al. 2006; Andreotti et al. 2013), defines a macroscopic cohesion  $c$ , and an internal  
 481 friction coefficient  $\mu_1^*$ , valid in simple shear for whatever normal stress  $\sigma_{22}$ . Here, assuming a  
 482 constant coefficient  $b$  in (17), the Mohr-Coulomb relation is predicted to hold with the same  
 483 value of internal friction as in the dry case,  $\mu_1^* = \mu_0^\infty$ , while macroscopic cohesion  $c$  is given  
 484 by

$$485 \quad c = \frac{b\mu_0^\infty F_0}{a^2} = \frac{b\pi\mu_0^\infty\Gamma}{a} \quad (19)$$

486 This estimate of the macroscopic cohesion in the Mohr-Coulomb sense is very similar to  
 487 the one obtained by Richefeu et al. (2006), by a different route. In Fig. 11, the prediction  
 488 of static friction coefficient  $\mu_0^*$  as a function of  $1/P^*$  using  $\beta$  as deduced from (17), with  
 489 coefficient  $b$  equal to the middle point of the specified interval, *viz.*  $b = \frac{(z_c+z)\Phi}{2\pi}$ , is shown to  
 490 perform quite well for  $P^* \geq 1$ , failing at small  $P^*$ , when the effective stress approach with  
 491 the exact value of  $\beta$  fails too.

492 In general, assuming a Mohr-Coulomb criterion for critical states to apply with a  $P^*$ -  
 493 independent value of cohesion  $c$  implies, upon dividing (18) by  $\sigma_{22} = P^*F_0/a^2$ , that the  
 494 quasistatic friction coefficient  $\mu_0^*$  should vary linearly with  $1/P^*$ :

$$495 \quad \mu_0^* = \frac{\sigma_{12}}{\sigma_{22}} = \mu_1^* + \frac{a^2c}{F_0P^*} \quad (20)$$

496 The Mohr-Coulomb representation of yield stresses might thus be used as an approximation  
 497 for  $P^* \geq 1$ , with  $a^2c/F_0 \simeq 0.27$ , but the observed sublinear increase of  $\mu_0^*$  with  $1/P^*$   
 498 in Fig. 11 (see the result for  $P^* = 0.436$ , and the subplot including value  $\mu_0^* \simeq 1.6$  for  
 499  $P^* = 0.1$ ) clearly precludes the definition of unique values of macroscopic cohesion and  
 500 friction coefficient according to (18) for smaller pressures.

## 501 CONCLUSIONS

502 We now provide a quick summary of the main results on both compression and steady  
 503 shear flow, and end with a discussion, in which perspectives for future work are evoked.

## 504 **Isotropic Compression**

505 Model wet granular assemblies exhibit the same striking differences with cohesionless sys-  
506 tems under compression that the simpler, mostly 2D models of the recent literature: stability  
507 of loose structures under low  $P^*$ , plastic behaviour in isotropic compression with hardening  
508 expressed by the overconsolidation pressure, linear variation of void ratio with  $\log P$  in some  
509 range – a qualitative behaviour common to many cohesive particulate materials. Compar-  
510 isons with experimental observations are possible. Although the sensitivity of the results to  
511 quite a few model features still needs to be assessed, one may tentatively conclude that the  
512 final state, obtained after sufficient overconsolidation, should be independent of the initial  
513 configurations and of some aspects of the compression procedure. This state is not affected  
514 by the removal of capillary forces, and may be regarded as the result of an ideal, homoge-  
515 neous and isotropic version of the moist tamping assembling process (Frost and Park 2003;  
516 Benahmed et al. 2004). It is looser (see Figs. 2(b) and 5) than directly compressed packs of  
517 dry grains, and could qualify as a reference loose state.

## 518 **Shear Flow and Critical States**

519 The main rheological influence of capillary adhesion on critical state and shear flow is a  
520 strong increase of shear resistance (or apparent friction  $\mu^*$ ) as  $P^*$  decreases, even though  
521 as  $P^*$  reaches values of order 0.1, the strong localization tendency hinders the identification  
522 of constitutive laws for homogeneous flow. Meanwhile, density and coordination numbers  
523 variations with  $P^*$  are slower. In the presence of capillary forces, clusters of particles joined  
524 by liquid bridges may survive strain intervals of several units, and the compressive role of  
525 attractive forces is not as immediately disturbed as the one of the externally applied normal  
526 stress upon increasing shear rate and inertial effects. A simple effective stress approach  
527 may quantitatively account for the shear resistance trend in good approximation as long as  
528  $P^* \geq 1$ . The Mohr-Coulomb criterion approximately describes critical states in the same  
529 reduced pressure range, but is no longer applicable at lower  $P^*$ . Many results (regarding,  
530 in particular, normal stress differences, fabric anisotropy, sensitivity to meniscus volume... )

531 are deferred to a more detailed paper submitted by some of the present authors (Khamseh  
532 et al. 2015). A major concern, the shear banding instability affecting low  $P^*$  shear flows,  
533 should certainly be addressed in a systematic study as well.

## 534 **Discussion**

535 Our simple model of wet grains reveals many new behaviors, compared to dry materials,  
536 and provides means for a critical review of macroscopic phenomenological laws (compression  
537 curve, Mohr-Coulomb criterion). While some phenomena were already explored in 2D  
538 cohesive models, modeling more realistic 3D systems reveals quantitative differences (e.g.,  
539 a much stronger enhancement of shear resistance), and should permit experimental con-  
540 frontations (Pierrat et al. 1998; Richefeu et al. 2006). The present paper did not discuss  
541 the influence of liquid saturation within the pendular range, and our model with constant  
542 meniscus volume does not strictly maintain a fixed water content in the material. Such  
543 issues are discussed separately for compression (Than et al. 2015) and shear flow (Khamseh  
544 et al. 2015) in forthcoming publications. We could check that a correction of the model in  
545 which capillary forces are slightly more accurately described does not significantly change  
546 the results. Similarly, a correction of meniscus volume to ensure a constant total liquid  
547 volume brings only hardly noticeable changes to compression or shear behavior. Rheological  
548 properties vary moderately through the pendular range (Khamseh et al. 2015) (with a very  
549 small density change and a variation of about 20% of  $\mu_0^*$  at  $P^* = 0.436$ ).

550 A more serious limitation of our model is its inability to deal with saturations exceeding  
551 the pendular regime. Numerical models for higher saturation levels, resorting, e.g., to a  
552 lattice Boltzmann discretization of the interstitial liquid, are currently being developed (De-  
553 lenne et al. 2015). Even in the small saturation range, though, the results for compression  
554 and shear show that the material behavior is considerably enriched compared to dry granular  
555 systems. One obvious, broad perspective is the exploration of the large unknown territory  
556 that separates isotropically assembled states from critical states, the simulation of deviatoric  
557 loads and the assessment of the applicability of macroscopic models of cohesive soils. It



558 would be interesting to explore the effects of resistance to rolling, due to surface asperities,  
559 on the material behavior in the presence of capillary cohesion. Even a small rolling resis-  
560 tance was observed to have important effects on the behavior of cohesive systems in two  
561 dimensions (Gilabert et al. 2008). It might be viewed as a first step towards the modeling of  
562 non-spherical objects (Estrada et al. 2011), but the geometry of liquid bridges joining objects  
563 with flat or angular surfaces might entail different force laws, and the effects of capillarity  
564 should be investigated in such cases.

## APPENDIX I. REFERENCES

- 565  
566 Agnolin, I. and Roux, J.-N. (2007a). “Internal states of model isotropic granular packings.  
567 I. Assembling process, geometry, and contact networks.” *Phys. Rev. E*, 76(6), 061302.
- 568 Agnolin, I. and Roux, J.-N. (2007b). “Internal states of model isotropic granular packings.  
569 II. Compression and pressure cycles.” *Phys. Rev. E*, 76(6), 061303.
- 570 Allen, M. and Tildesley, D. (1987). *Computer simulations of liquids*. Oxford University Press,  
571 Oxford.
- 572 Andreotti, B., Forterre, Y., and Pouliquen, O. (2013). *Granular Media: Between Fluid and*  
573 *Solid*. Cambridge University Press, Cambridge, UK.
- 574 Azéma, E. and Radjaï, F. (2014). “Internal structure of inertial granular flows.” *Phys. Rev.*  
575 *Lett.*, 112, 078001.
- 576 Azéma, E., Radjaï, F., and Dubois, F. (2013). “Packings of irregular polyhedral particles:  
577 Strength, structure, and effects of angularity.” *Phys. Rev. E*, 87, 062223.
- 578 Azéma, E., Radjaï, F., and Roux, J.-N. (2015). “Internal friction and absence of dilatancy  
579 of packings of frictionless polygons.” *Phys. Rev. E*, 91, 010202(R).
- 580 Benahmed, N., Canou, J., and Dupla, J.-C. (2004). “Structure initiale et propriétés de  
581 liquéfaction statique d’un sable.” *Comptes-Rendus Académie des Sciences, Mécanique*,  
582 332, 887–894.
- 583 Biarez, J. and Hicher, P.-Y. (1993). *Elementary Mechanics of Soil Behaviour*. A. A. Balkema,  
584 Rotterdam.
- 585 Bruchon, J.-F., Pereira, J.-M., Vandamme, M., Lenoir, N., Delage, P., and Bornert, M.  
586 (2013a). “Full 3d investigation and characterisation of capillary collapse of a loose unsat-  
587 urated sand using x-ray ct..” *Granular Matter*, 15(6), 783–800.
- 588 Bruchon, J.-F., Pereira, J.-M., Vandamme, M., Lenoir, N., Delage, P., and Bornert, M.  
589 (2013b). “X-ray microtomography characterisation of the changes in statistical homogene-  
590 ity of an unsaturated sand during imbibition..” *Géotechnique Letters*, 3, 84–88.
- 591 Cumberland, D. and Crawford, R. (1987). *The Packing of Particles*. Elsevier, Amsterdam.

592 da Cruz, F., Emam, S., Prochnow, M., Roux, J.-N., and Chevoir, F. (2005). “Rheophysics  
593 of dense granular materials: discrete simulation of plane shear flows.” *Phys. Rev. E*, 72,  
594 021309.

595 Delenne, J.-Y., Richefeu, V., and Radjaï, F. (2015). “Liquid clustering and capillary pressure  
596 in granular media.” *J. Fluid Mech.*, 762, R5.

597 Donev, A., Torquato, S., and Stillinger, F. H. (2005). “Pair correlation function character-  
598 istics of nearly jammed disordered and ordered hard-sphere solids.” *Phys. Rev. E*, 71(1),  
599 011105.

600 Elata, D. and Berryman, J. G. (1996). “Contact force-displacement laws and the mechanical  
601 behavior of random packs of identical spheres.” *Mechanics of Materials*, 24, 229–240.

602 Estrada, N., Azéma, E., Radjaï, F., and Taboada, A. (2011). “Identification of rolling resis-  
603 tance as a shape parameter in sheared granular media..” *Phys. Rev. E*, 84, 011306.

604 Forterre, Y. and Pouliquen, O. (2008). “Flows of dense granular media.” *Annu. Rev. Fluid  
605 Mech.*, 40, 1–24.

606 Frost, J. D. and Park, J.-Y. (2003). “A critical assessment of the moist tamping technique.”  
607 *ASTM Geotechnical Testing Journal*, GTJ20039850–261.

608 Gilabert, F. A., Roux, J.-N., and Castellanos, A. (2007). “Computer simulation of model  
609 cohesive powders: Influence of assembling procedure and contact laws on low consolidation  
610 states.” *Phys. Rev. E*, 75(1), 011303.

611 Gilabert, F. A., Roux, J.-N., and Castellanos, A. (2008). “Computer simulation of model  
612 cohesive powders: Plastic consolidation, structural changes, and elasticity under isotropic  
613 loads.” *Phys. Rev. E*, 78(1), 031305.

614 Hatano, T. (2007). “Power-law friction in closely packed granular materials.” *Phys. Rev. E*,  
615 75, 060301(R).

616 Herminghaus, S. (2005). “Dynamics of wet granular matter.” *Advances in Physics*, 54, 3,  
617 221–261.

618 Khamseh, S., Roux, J.-N., and Chevoir, F. (2015). “Flow of wet granular materials: a

619 numerical study.”, submitted for publication in *Phys. Rev. E*.

620 Kohonen, M. M., Geromichalos, D., Scheel, M., Schier, C., and Herminghaus, S. (2004). “On  
621 capillary bridges in wet granular materials.” *Physica A*, 339, 7–15.

622 Kruyt, N. P. and Rothenburg, L. (2014). “On micromechanical characteristics of the critical  
623 state of two-dimensional granular materials.” *Acta Mechanica*, 225(8), 2301 – 2318.

624 Kudrolli, A. (2008). “Granular matter: Sticky sand.” *Nature Materials*, 7, 174–175.

625 Lian, G., Thornton, C., and Adams, M. (1993). “A theoretical-study of the liquid bridge  
626 forces between 2 rigid spherical bodies.” *J. Coll. Inter. Sci.*, 161, 138–147.

627 Magnanimo, V., La Ragione, L., Jenkins, J. T., Wang, P., and Makse, H. A. (2008). “Char-  
628 acterizing the shear and bulk moduli of an idealized granular material.” *Europhys. Lett.*,  
629 81, 34006.

630 Maugis, D. (1987). “Adherence of elastomers: Fracture mechanics aspects.” *Journal of Ad-  
631 hesion Science and Technology*, 1, 105–134.

632 Mitarai, N. and Nori, F. (2006). “Wet granular materials.” *Advances in Physics*, 55, 1, 1–45.

633 Mitchell, J. and Soga, K. (2005). *Fundamentals of Soil Behavior*. Wiley.

634 O’Hern, C., Silbert, L. E., Liu, A. J., and Nagel, S. R. (2003). “Jamming at zero temperature  
635 and zero applied stress: The epitome of disorder.” *Phys. Rev. E*, 68(1), 011306.

636 Peyneau, P.-E. and Roux, J.-N. (2008a). “Frictionless bead packs have macroscopic friction,  
637 but no dilatancy.” *Phys. Rev. E*, 78, 011307.

638 Peyneau, P.-E. and Roux, J.-N. (2008b). “Solidlike behavior and anisotropy in rigid friction-  
639 less bead assemblies.” *Phys. Rev. E*, 78, 041307.

640 Pierrat, P., Agrawal, D. K., and Caram, H. S. (1998). “Effect of moisture on the yield locus  
641 of granular materials: theory of shift.” *Powder Tech.*, 99, 220–227.

642 Pitois, O., Moucheron, P., and Chateau, X. (2000). “Liquid bridge between two moving  
643 spheres: An experimental study of viscosity effects.” *J. Coll. Interf. Sci.*, 231, 26–31.

644 Radjai, F., Delenne, J.-Y., Azéma, E., and Roux, S. (2012). “Fabric evolution and accessible  
645 geometrical states in granular materials.” *Granular Matter*, 14, 259–264.

646 Radjaï, F. and Dubois, F. (2011). *Discrete-element modeling of granular materials*. Wiley.

647 Radjaï, F. and Richefeu, V. (2009). “Bond anisotropy and cohesion of wet granular materi-  
648 als.” *Phil. Trans. R. Soc. A*, 367, 5123–5138.

649 Radjaï, F., Troadec, H., and Roux, S. (2004). “Basic features of granular plasticity.” *Granular*  
650 *Materials: Fundamentals and Applications*, S. J. Antony, W. Hoyle, and Y. Ding, eds.,  
651 Cambridge, Royal Society of Chemistry, 157–183.

652 Richefeu, V., El Youssoufi, M., and Radjaï, F. (2006). “Shear strength properties of wet  
653 granular materials.” *Phys. Rev. E*, 73, 051304.

654 Rognon, P., Roux, J.-N., Naaïm, M., and Chevoir, F. (2008). “Dense flows of cohesive  
655 granular materials.” *J. Fluid Mech.*, 596, 21–47.

656 Rognon, P., Roux, J.-N., Wolf, D., Naaïm, M., and Chevoir, F. (2006). “Rheophysics of  
657 cohesive granular materials.” *Europhysics Letters*, 74, 644–650.

658 Rothenburg, L. and Kruyt, N. P. (2004). “Critical state and evolution of coordination number  
659 in simulated granular materials.” *International Journal of Solids and Structures*, 41(2),  
660 5763–5774.

661 Roux, J.-N. and Chevoir, F. (2011). “Dimensional Analysis and Control Parameters.” In  
662 (Radjaï and Dubois 2011), Chapter 8, 199–232.

663 Saint-Cyr, B., Szarf, K., Voivret, C., Azéma, E., Richefeu, V., Delenne, J.-Y., Combe, G.,  
664 Nouguièr-Lehon, C., Villard, P., Sornay, P., Chaze, M., and Radjaï, F. (2012). “Particle  
665 shape dependence in 2d granular media.” *EPL*, 98(4), 44008.

666 Scholtès, L., Chareyre, B., Nicot, F., and Darve, F. (2009a). “Micromechanics of granular  
667 materials with capillary effects.” *International Journal of Engineering Science*, 47, 64–75.

668 Scholtès, L., Hicher, P.-Y., Nicot, F., Chareyre, B., and Darve, F. (2009b). “On the capillary  
669 stress tensor in wet granular materials.” *Int. Journal for Numerical and Analytical Methods*  
670 *in Geomechanics*, 33, 1289–1313.

671 Silbert, L. E., Ertas, D., Grest, G. S., Halsey, T. C., and Levine, D. (2002). “Geometry of  
672 frictionless and frictional sphere packings.” *Phys. Rev. E*, 65(3), 031304.

- 673 Soulié, F., Cherblanc, F., El Youssoufi, M., and Saix, C. (2006). “Influence of liquid bridges  
674 on the mechanical behaviour of polydisperse granular materials.” *Int. J. Numer. Anal.*  
675 *Meth. Geomech.*, 30, 213–228.
- 676 Than, V.-D., Roux, J.-N., Tang, A. M., and Pereira, J.-M. (2015). “Numerical simulation of  
677 plastic compression of wet granular soils.”, to be submitted.
- 678 Thornton, C. (2000). “Numerical simulations of deviatoric shear deformation of granular  
679 media.” *Géotechnique*, 50, 43–53.
- 680 Willett, C., Adams, M., Johnson, S., and Seville, J. (2000). “Capillary bridges between two  
681 spherical bodies.” *Langmuir*, 16 (24), 9396–9405.
- 682 Wood, D. M. (1990). *Soil Behaviour and Critical State Soil Mechanics*. Cambridge University  
683 Press.

684

**APPENDIX II. NOTATION**

685

*The following symbols are used in this paper:*

686

 $a$  = spherical grain diameter; $\alpha$  = exponent of power law expressing internal friction increase with  $I$ ; $b$  = proportionality coefficient relating  $\beta$  to  $1/P^*$ ; $\beta$  = ratio of capillary contribution to total normal stress in shear flow; $C$  = coefficient of  $I^\alpha$  for power law increase of  $\mu^*$ ; $c$  = macroscopic cohesion according to Mohr-Coulomb criterion; $D_0$  = rupture distance of liquid bridge; $\tilde{E}$  = Modulus appearing in Hertz law; $e$  = void ratio; $e_0$  = void ratio in critical state; $e_{\text{iso}}$  = void ratio in isotropic compression;

687

 $F_0$  = maximum capillary tensile force through liquid bridge; $\Phi$  = solid fraction; $\Phi_0$  = solid fraction in critical state; $\Phi_{\text{iso}}$  = solid fraction in isotropic compression; $\varphi$  = filling angle in liquid meniscus; $\Gamma$  = surface tension of nonsaturating interstitial liquid; $\dot{\gamma}$  = shear rate; $h$  = distance between particles or contact deflection; $I$  = inertial number; $\kappa$  = dimensionless contact stiffness number; $m$  = grain mass;

- $\mu$  = intergranular friction coefficient;  
 $\mu^*$  = apparent internal, macroscopic friction coefficient;  
 $\mu_1^*$  = internal friction coefficient according to Mohr-Coulomb criterion;  
 $\mu_0^\infty$  = internal friction coefficient in critical state for dry grains;  
 $\Omega$  = total sample volume;  
 $\Omega_l$  = liquid volume;  
 $P$  = controlled stress: isotropic pressure in compression, normal stress  $\sigma_{22}$  in shear flow;  
 $P^*$  = dimensionless, reduced pressure;  
 $\mathcal{P}$  = mean pressure;  
 $S$  = saturation;  
 $\sigma_{\alpha\beta}$  = stress tensor;  
 $\sigma_{\alpha\beta}^{\text{eff}}$  = effective stress tensor;  
 $\sigma_{\alpha\beta}^{\text{cap}}$  = contribution of all capillary forces to stress tensor;  
 $\sigma_{\alpha\beta}^{\text{T}}$  = contribution of tangential forces to stress tensor;  
 $\sigma_{\alpha\beta}^{\text{N}}$  = contribution of normal forces to stress tensor;  
 $\sigma_{\alpha\beta}^{\text{c}}$  = contribution of contact forces to stress tensor;  
 $\sigma_{\alpha\beta}^{\text{Ne}}$  = contribution of normal, elastic contact forces to stress tensor;  
 $\sigma_{\alpha\beta}^{\text{N,c}}$  = contribution of capillary forces in contacts to stress tensor;  
 $\sigma_{\alpha\beta}^{\text{d}}$  = contribution of distant capillary forces to stress tensor;  
 $V$  = meniscus volume;  
 $V_0$  = initial mean quadratic agitation velocity, in assembling stage;  
 $V^*$  = characteristic velocity, associated with attractive force;  
 $z_c$  = coordination number of contacts;  
 $z_d$  = coordination number of distant interactions;  
 $z$  = total coordination number.



**List of Figures**

690	1	A meniscus between two spherical grains of diameter $a = 2R$ , with distance	
691		$h$ between solid surfaces, filling angle $\varphi$ , contact angle $\theta$ . . . . .	31
692	2	(a) Effect of cycle of pressure (in dimensionless form) on void ratio. The	
693		straight line fits the curve for intermediate $P^*$ values. (b) Same curve, com-	
694		pared to result obtained with dry, cohesionless grains (bottom curve, crosses	
695		joined by dark line), with pressure in kPa, for glass beads with $a = 0.115$ mm,	
696		wet by water. . . . .	32
697	3	Effect of different (isotropic) unloading and reloading histories on void ratio.	
698		The system does not rearrange along unloading paths $BB'$ , $CC'$ , $DD'$ , $EE'$ ,	
699		which are reversible. Path 5 causes plastic response in section CE, along	
700		which pressure increases beyond its past maximum. The primary curve (path	
701		4) is then retraced. . . . .	33
702	4	Evolution of coordination numbers of contacts $z_c$ and of distant interactions	
703		$z_d$ , in the pressure cycle of Fig. ??(a). . . . .	34
704	5	Void ratio versus reduced pressure $P^*$ , as cohesive forces are suppressed at the	
705		beginning of unloading, starting at different points on the primary compression	
706		curve. (In this case the initial state had solid fraction $\Phi_0 = 0.45$ ). . . . .	35
707	6	(a) Internal friction coefficient $\mu^*$ and (b) solid fraction $\Phi$ versus $I$ for different	
708		values of $P^*$ . . . . .	36
709	7	Main plot: void ratios in primary isotropic compression, $e_{\text{iso}}$ (square dots),	
710		and in critical state, $e_0$ (crosses with error bars) versus $\log P^*$ . Inset: detail	
711		of variations of <i>solid fraction</i> $\Phi_{\text{iso}}$ in isotropic compression (square dots), and	
712		$\Phi_0$ , in critical state (crosses), for large $P^*$ (including the dry case of infinite	
713		$P^*$ ), versus $1/P^*$ . Dashed lines are drawn to guide the eye. . . . .	37

714	8	Coordination numbers of contacts $z_c$ (left axis, upper curves) and of distant interactions $z_d$ (right axis, bottom curves), versus reduced pressure for different values of $I$ . . . . .	38
715			
716			
717	9	Contribution of capillary forces to normal stress $\sigma_{22}$ . . . . .	39
718	10	Distribution of the age of menisci for different $P^*$ values (results for different $I$ indistinguishable on this plot). Inset shows detail of initial decay. . . . .	40
719			
720	11	Apparent quasistatic friction coefficient $\mu_0^*$ versus $1/P^*$ – showing the value of $\mu_0^\infty$ for $1/P^* = 0$ . Square dots: numerical results (error bars are smaller); (red) crosses: predictions of (??), with exact coefficient $\beta$ ; (blue) circles: same with estimated $\beta$ . Dotted lines: Mohr-Coulomb models, predicted from (??) (upper line), or fitted to the data in range $P^* \geq 1$ (lower straight line). Inset: measured $\mu_0^*$ versus $1/P^*$ , including data point for $P^* = 0.1$ , with Mohr-Coulomb fit to $P^* \geq 1$ data. . . . .	41
721			
722			
723			
724			
725			
726			

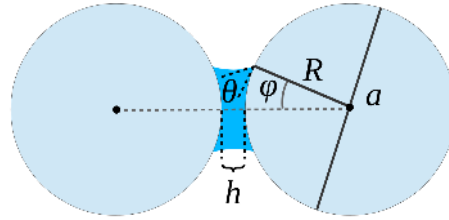


**FIG. 1.** A meniscus between two spherical grains of diameter  $a = 2R$ , with distance  $h$  between solid surfaces, filling angle  $\varphi$ , contact angle  $\theta$ .

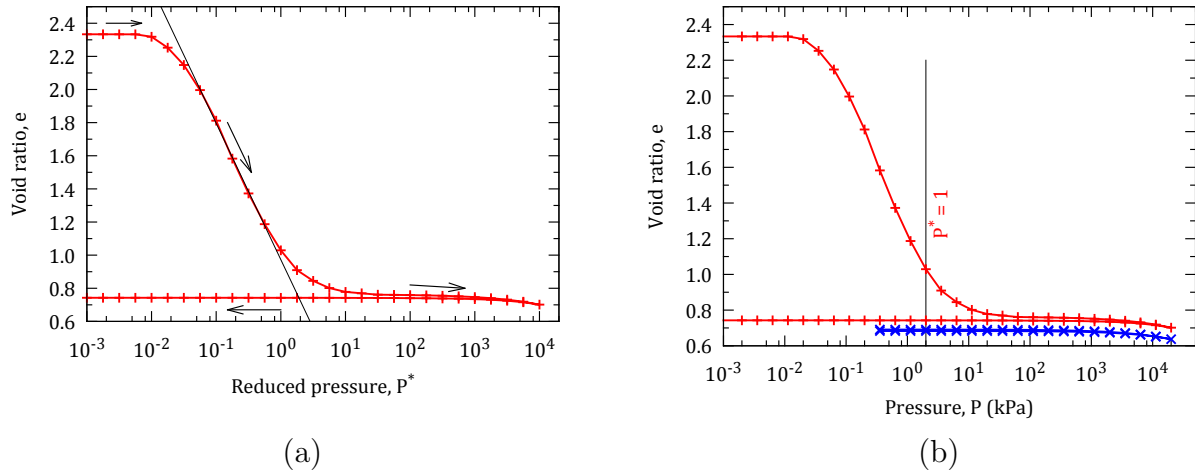


**FIG. 2. (a) Effect of cycle of pressure (in dimensionless form) on void ratio. The straight line fits the curve for intermediate  $P^*$  values. (b) Same curve, compared to result obtained with dry, cohesionless grains (bottom curve, crosses joined by dark line), with pressure in kPa, for glass beads with  $a = 0.115$  mm, wet by water.**

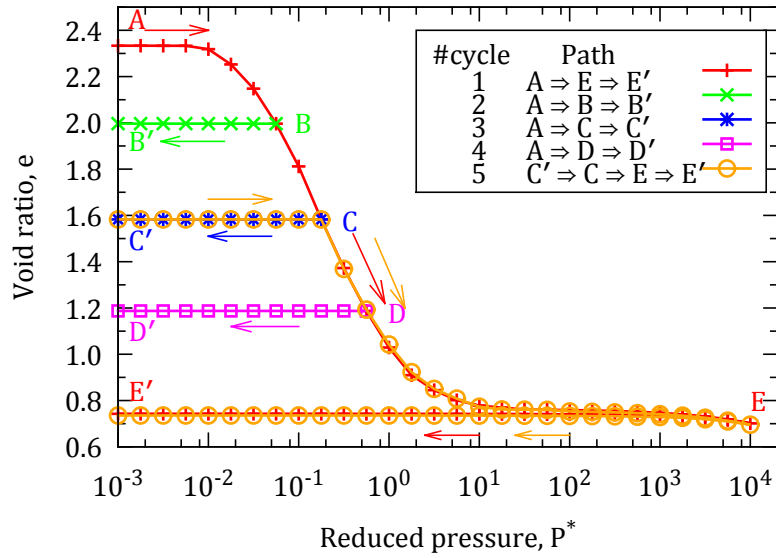


**FIG. 3. Effect of different (isotropic) unloading and reloading histories on void ratio. The system does not rearrange along unloading paths  $BB'$ ,  $CC'$ ,  $DD'$ ,  $EE'$ , which are reversible. Path 5 causes plastic response in section CE, along which pressure increases beyond its past maximum. The primary curve (path 4) is then retraced.**

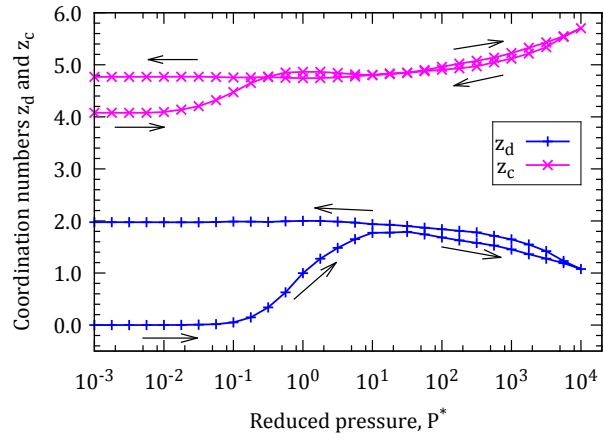


**FIG. 4.** Evolution of coordination numbers of contacts  $z_c$  and of distant interactions  $z_d$ , in the pressure cycle of Fig. 2(a).

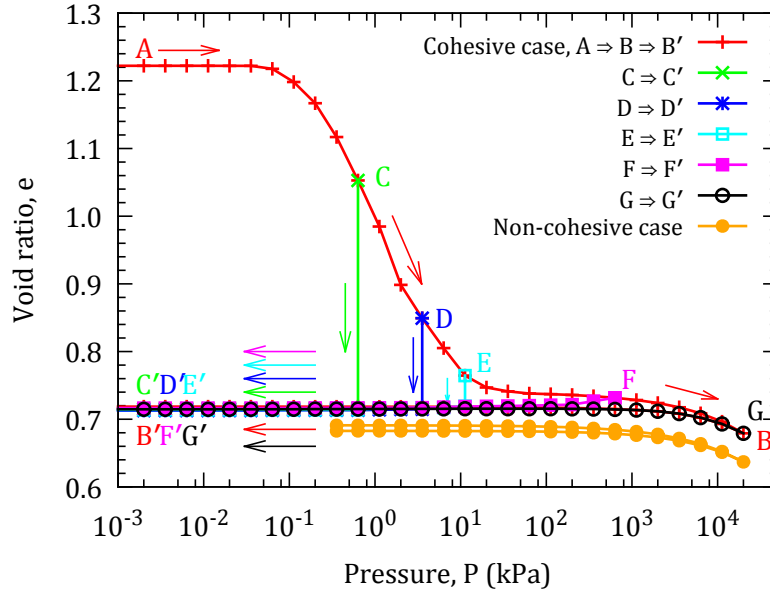


**FIG. 5. Void ratio versus reduced pressure  $P^*$ , as cohesive forces are suppressed at the beginning of unloading, starting at different points on the primary compression curve. (In this case the initial state had solid fraction  $\Phi_0 = 0.45$ ).**

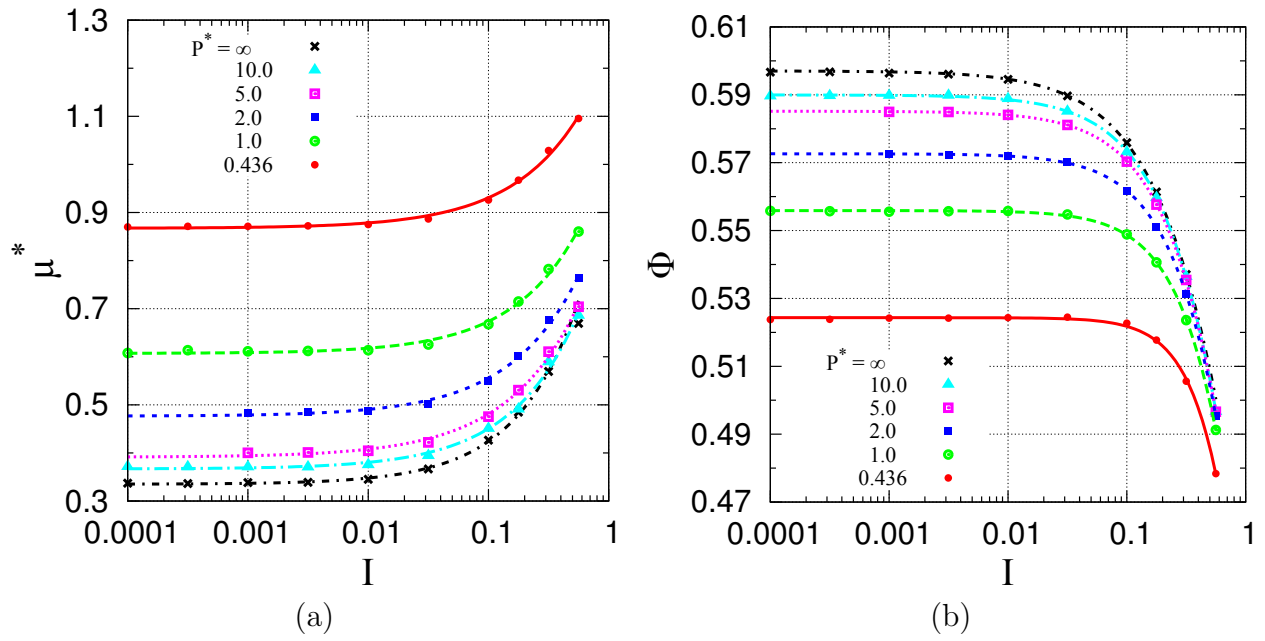
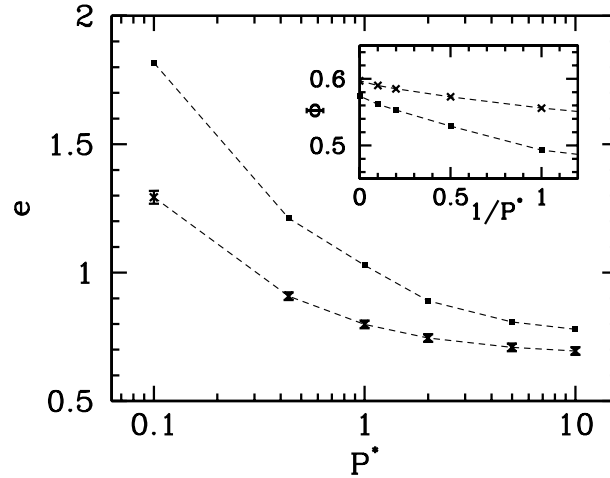
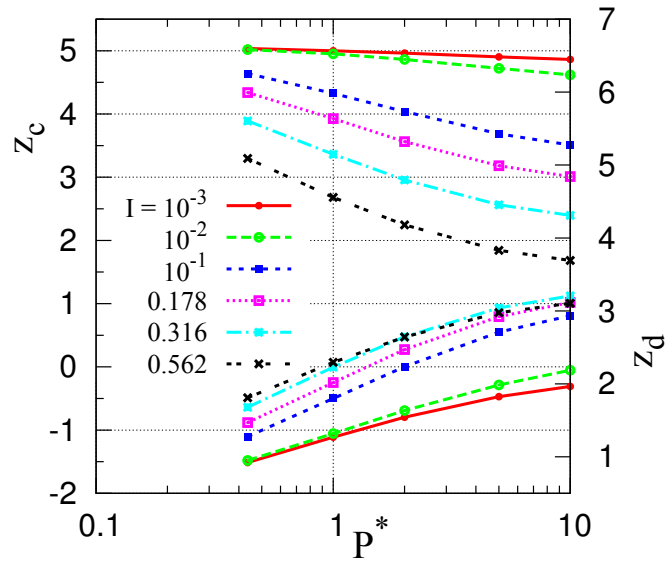


FIG. 6. (a) Internal friction coefficient  $\mu^*$  and (b) solid fraction  $\Phi$  versus  $I$  for different values of  $P^*$ .





**FIG. 7.** Main plot: void ratios in primary isotropic compression,  $e_{\text{iso}}$  (square dots), and in critical state,  $e_0$  (crosses with error bars) versus  $\log P^*$ . Inset: detail of variations of solid fraction  $\Phi_{\text{iso}}$  in isotropic compression (square dots), and  $\Phi_0$ , in critical state (crosses), for large  $P^*$  (including the dry case of infinite  $P^*$ ), versus  $1/P^*$ . Dashed lines are drawn to guide the eye.



**FIG. 8.** Coordination numbers of contacts  $z_c$  (left axis, upper curves) and of distant interactions  $z_d$  (right axis, bottom curves), versus reduced pressure for different values of  $I$ .

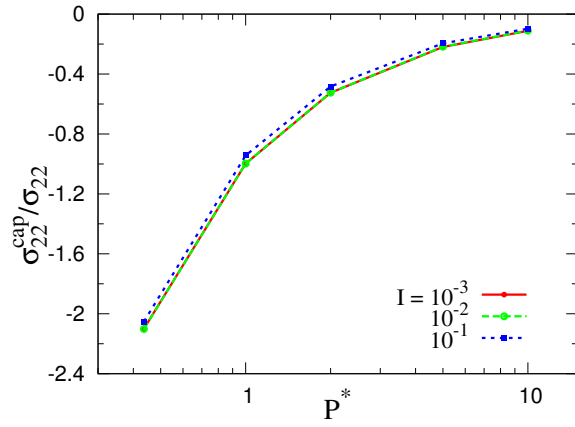


**FIG. 9. Contribution of capillary forces to normal stress  $\sigma_{22}$ .**

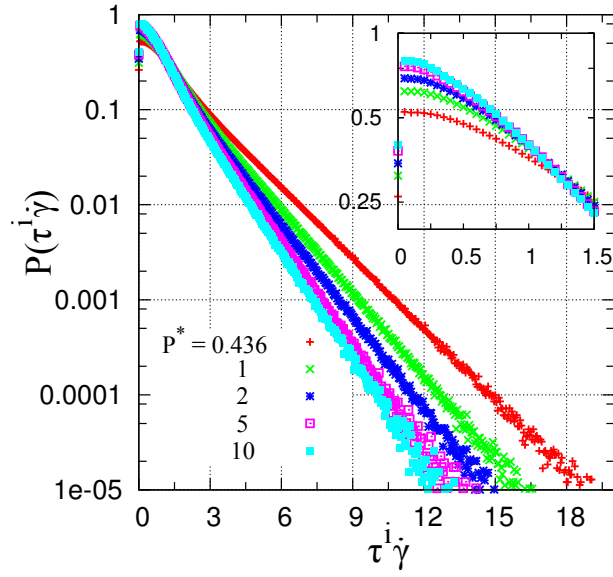


**FIG. 10.** Distribution of the age of menisci for different  $P^*$  values (results for different  $I$  indistinguishable on this plot). Inset shows detail of initial decay.

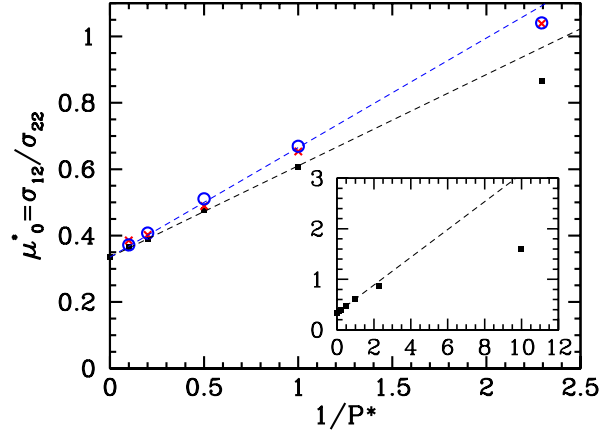


**FIG. 11.** Apparent quasistatic friction coefficient  $\mu_0^*$  versus  $1/P^*$  – showing the value of  $\mu_0^\infty$  for  $1/P^* = 0$ . Square dots: numerical results (error bars are smaller); (red) crosses: predictions of (14), with exact coefficient  $\beta$ ; (blue) circles: same with estimated  $\beta$ . Dotted lines: Mohr-Coulomb models, predicted from (19) (upper line), or fitted to the data in range  $P^* \geq 1$  (lower straight line). Inset: measured  $\mu_0^*$  versus  $1/P^*$ , including data point for  $P^* = 0.1$ , with Mohr-Coulomb fit to  $P^* \geq 1$  data.